

# Impact of measurement precision and noise on superresolution image reconstruction

Sally L. Wood,<sup>1,\*</sup> Shu-Ting Lee,<sup>1</sup> Gao Yang,<sup>1</sup> Marc P. Christensen,<sup>2</sup> and Dinesh Rajan<sup>2</sup>

<sup>1</sup>Department of Electrical Engineering, Santa Clara University, 500 El Camino, Santa Clara, California 95053, USA

<sup>2</sup>Department of Electrical Engineering, Southern Methodist University, 6251 Airline Road, Dallas, Texas 75275, USA

\*Corresponding author: swood@scu.edu

Received 13 September 2007; revised 2 January 2008; accepted 24 February 2008;  
posted 25 February 2008 (Doc. ID 87509); published 31 March 2008

The performance of uniform and nonuniform detector arrays for application to the PANOPTES (processing arrays of Nyquist-limited observations to produce a thin electro-optic sensor) flat camera design is analyzed for measurement noise environments including quantization noise and Gaussian and Poisson processes. Image data acquired from a commercial camera with 8 bit and 14 bit output options are analyzed, and estimated noise levels are computed. Noise variances estimated from the measurement values are used in the optimal linear estimators for superresolution image reconstruction. © 2008 Optical Society of America

OCIS codes: 110.0110, 100.6640.

## 1. Introduction

The objective of superresolution image reconstruction of a high resolution (HR) image from multiple low resolution (LR) images is to computationally create a high quality sampled image at a resolution greater than the resolution of LR imaging devices. This problem is motivated by a variety of applications with different performance measures and constraints. With traditional digital image acquisition methods, a detector array samples the image projected onto a detector plane to produce a directly usable image at the resolution of the detector array. In contrast, computational imaging techniques use the information from a set of LR images, each of which individually may have little value. However, if the set of LR images contains sufficient information for the desired HR image, estimation methods may be applied. The performance of these methods depends on the noise environment and the accuracy and variability of the modeling assumptions.

In Chaudhuri [1], a number of authors describe a wide range of algorithms and applications. There are

two basic approaches to acquiring a set of LR images. In one the set is acquired sequentially from a single mobile low resolution camera [2–4], so a simple low-cost camera can be used to create images with the same high resolution as a more expensive camera. Reconstruction methods using a set of translated images are described by Elad [2,3] and Farsiu *et al.* [4]. A fundamental problem for this type of application, the accurate relative registration of the LR image set, is addressed by Vandewalle *et al.* [5] and Robinson *et al.* [6].

Alternatively, the LR image set may be acquired simultaneously from an array of subimaging units designed for a computational imaging device. The look directions of the subimagers may be fixed or controllable. Tanida *et al.* [7] describe the TOMBO (thin observation module by bound optics) architecture and early experiments using a small set of subimagers, each having a small detector array and a fixed microlens. Kitamura *et al.* [8] and Nitta *et al.* [9] have reported improvements in the design and reconstruction algorithms. Christensen *et al.* [10] propose a steerable micromirror array in the PANOPTES (processing arrays of Nyquist-limited observations to produce a thin electro-optic sensor) design to avoid the limited operational range of a fixed compound

eye design. The mirrors control overlapping subimager fields of view, which allows variable resolution improvement. In addition, dynamically responding to the local entropy of the imaged scene allows efficient allocation of subimager resources [10]. Wood *et al.* [11,12] and Lan *et al.* [13] have shown that reconstruction performance can be improved by augmenting uniform subimager detector arrays with arrays with a diversity of magnifications and orientations. This reduces and decouples computation and also can extend the dynamic operational range of super-resolution devices to detect low contrast objects beyond the 8-bit dynamic range designed for human viewing. For example, computational imaging methods in radio astronomy and medical imaging [14–16] can produce image content with a wide dynamic range that may be viewed with a user selected display range or may be processed automatically.

Plans for construction and preliminary testing of the PANOPTES data acquisition system and testing of the measurement model for reconstruction algorithms were recently reported by Wood *et al.* [17]. This paper considers the previously reported theoretical performance of uniform and diverse detector arrays [11–13] in the context of quantization and Poisson distributed noise. It analyzes data acquired from a monochromatic commercial camera that provides 8-bit and 14-bit video graphics array (VGA) resolution image data and compares results to model assumptions used in the development of image reconstruction algorithms. Using this quantitative investigation of a typical noise environment provides useful information for both reconstruction algorithm and sensor architecture decisions. The next section briefly describes the noise model and the data acquisition model based on a continuous source model. The different effects of aliasing and spatial frequency attenuation in acquired LR images are specified. Following that section, the linear reconstruction methods for space variant and diverse sensor systems are considered in the context of expected levels of noise due to quantization and Poisson processes in addition to Gaussian noise. The fourth section uses image sequences to compute image variability and uses a standard resolution test chart as the image target. The concluding section discusses the implications of a large Poisson distributed contribution to measurement variance and spatial and temporal variability of measurement acquisition on the expected performance of reconstruction algorithms.

## 2. Data Acquisition and Noise Models

The underlying source model for many superresolution image reconstruction formulations is a pixelated source at a desired resolution captured by an array of lower resolution identical detectors operating under constant environmental conditions. From this basic model the effects of higher resolution source models, nonuniform detector arrays, and variable operating conditions can be examined.

### A. Measurement Model

In a typical image acquisition model (e.g., [18,19]) a continuous image intensity pattern,  $f_C(x, y)$ , is projected onto the detector plane of a camera with a spatial resolution determined by the optics of the camera's lens system. The discrete sampled image,  $g(m_x, m_y)$ , is created by an array of detectors as shown in the block diagram in Fig. 1, where the detector blur and sampling are shown as two separate blocks. Information from  $f_C(x, y)$  can be lost in the creation of the discrete image due to attenuation of spatial frequencies by the convolution in the first block or aliasing in the second. Exact recovery of  $f_C(x, y)$  from the continuous function  $g_C(x, y)$  requires an inverse convolution, but often this inverse is ill-conditioned and sensitive to added measurement noise. A single discrete image  $g(m_x, m_y)$  in general contains aliased spatial frequencies from  $g_C(x, y)$ , and in the typical superresolution application (e.g., [1]), the effective sampling interval is reduced by acquiring multiple sampled images with lateral shifts of fractions of a pixel width prior to sampling.

These relationships are illustrated in Figs. 2 and 3. Figure 2(a) shows a  $480 \times 640$  pixel image of part of the high contrast 1951 US Air Force (USAF) resolution test chart used in this paper to evaluate noise components of measurements and the expected effect of the noise on reconstruction performance. The chart contains groups of vertical columns with six sets of horizontal and vertical bar patterns. The number above each group column indicates a relative power of 2 for the scaling factor. Although other standard resolution test patterns may better demonstrate modulation transfer functions and natural images show subjective characteristics of reconstructed images, this pattern was selected to provide a simple direct measure of two element discrimination based on the difference between the maximum and minimum pixel values in an element in original and reconstructed images. For reference, Fig. 2(b) shows an enlargement of the 200 pixel square area for groups 0 and 1, and Fig. 2(c) shows the 50 pixel square area for groups 2 and 3. Element 1-5 has a height of 10 pixels, which is the smallest size that will guarantee that some pixels will be completely

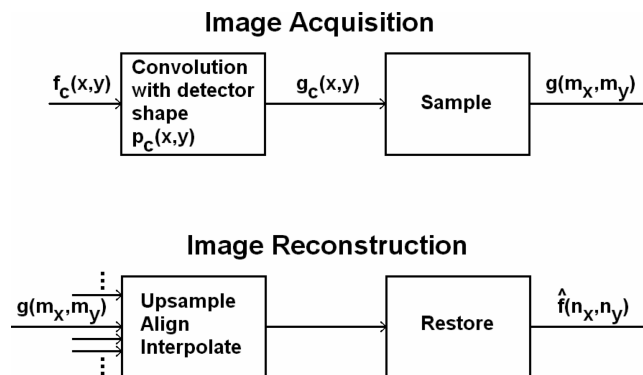
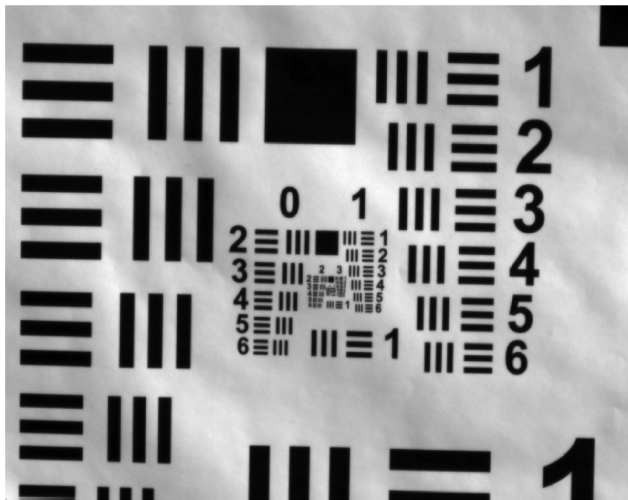
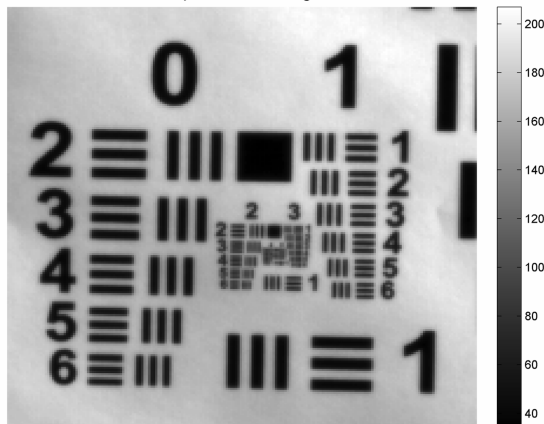


Fig. 1. Block diagram of image acquisition and reconstruction.



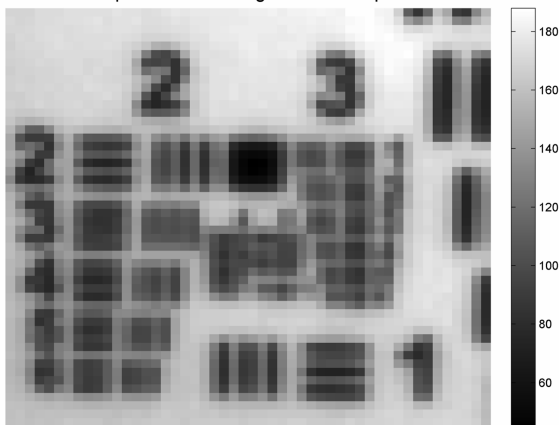
(a)

Groups 0 and 1 Original



(b)

Groups 2 and 3 of Original: 50 x 50 pixels



(c)

Fig. 2. (a) Mean value of 300 480 × 640 pixel images of 1951 U.S. Air Force resolution test chart; (b) magnified 200 × 200 pixel section of a single frame showing groups 0 and 1; (c) magnified 50 × 50 pixel section of a single frame showing groups 2 and 3.

in the black or white region regardless of translations. In group 2 the elements show aliasing and blurring, and in group 3 the individual elements are not distinguishable.

The different effects of blurring and aliasing in a noise free environment can be simulated using a single image, and these controlled results can be used as a basis for comparison with results of computationally increasing the resolution using multiple images. A single image at the resolution shown in Fig. 2(a) was computationally reduced in resolution by a factor of 4 to simulate LR images from a larger detector size. Then, 16 shifted LR images were up-sampled and aligned to create a higher resolution image with an effective sampling frequency increased by a factor of 4 compared to the LR image. Two LR images of groups 0 and 1 at different translation positions are shown in Figs. 3(a) and 3(b) to illustrate the shift dependent variability of the aliased images. These images have a resolution similar to the image of groups 2 and 3 of the original image shown in Fig. 2(c). The computed result in Fig. 3(c) is the equivalent of  $g_C(x, y)$  sampled at four times the rate used for the LR images. With this reduction in aliasing, the improvement in the smaller elements of group 0 is visually apparent. This noise free simulation result will be compared to a similar process applied to a sequence of acquired images with estimates of the noise variance.

In Fig. 3(d) the pixel values along a vertical column through the horizontal lines of groups 0 are shown for the computed image in Fig. 3(c) (solid curve) and the original image at the same resolution (dotted curve). For reference the corresponding column from the original group 2 is plotted with round markers with the horizontal scale adjusted by a factor of 4 to align the element boundaries with the other two plots. Profiles through group 0 of the computed LR images are not shown, but are similar to the group 2 profile. The improvement is due to effectively increasing the sampling rate to avoid aliasing by acquiring and aligning multiple LR images. This computation is not sensitive to measurement noise if the alignment can be accurately determined, although the presence of noise will generally degrade the image quality. The expected effects of pixel width blurring remain in the computed image profile, with attenuation increasing as the size of the element bars decreases. Compensation for this blurring to restore attenuated spatial frequencies in the original image is highly sensitive to amplification of added noise in spatial frequency regions with high attenuation due to the blur [18,19].

#### B. Sources of Measurement Noise

The three most likely sources of added measurement noise are quantization due to a fixed number of bits in the LR image acquisition, Poisson counting statistics of the number of photoelectrons generated at the detector, and other random variations in the measurement acquisition process. Other sources of inaccuracies include variations in individual detector responses, variations in illumination level, and incorrect modeling of the detector array response. In order to easily compare measurement variance from a

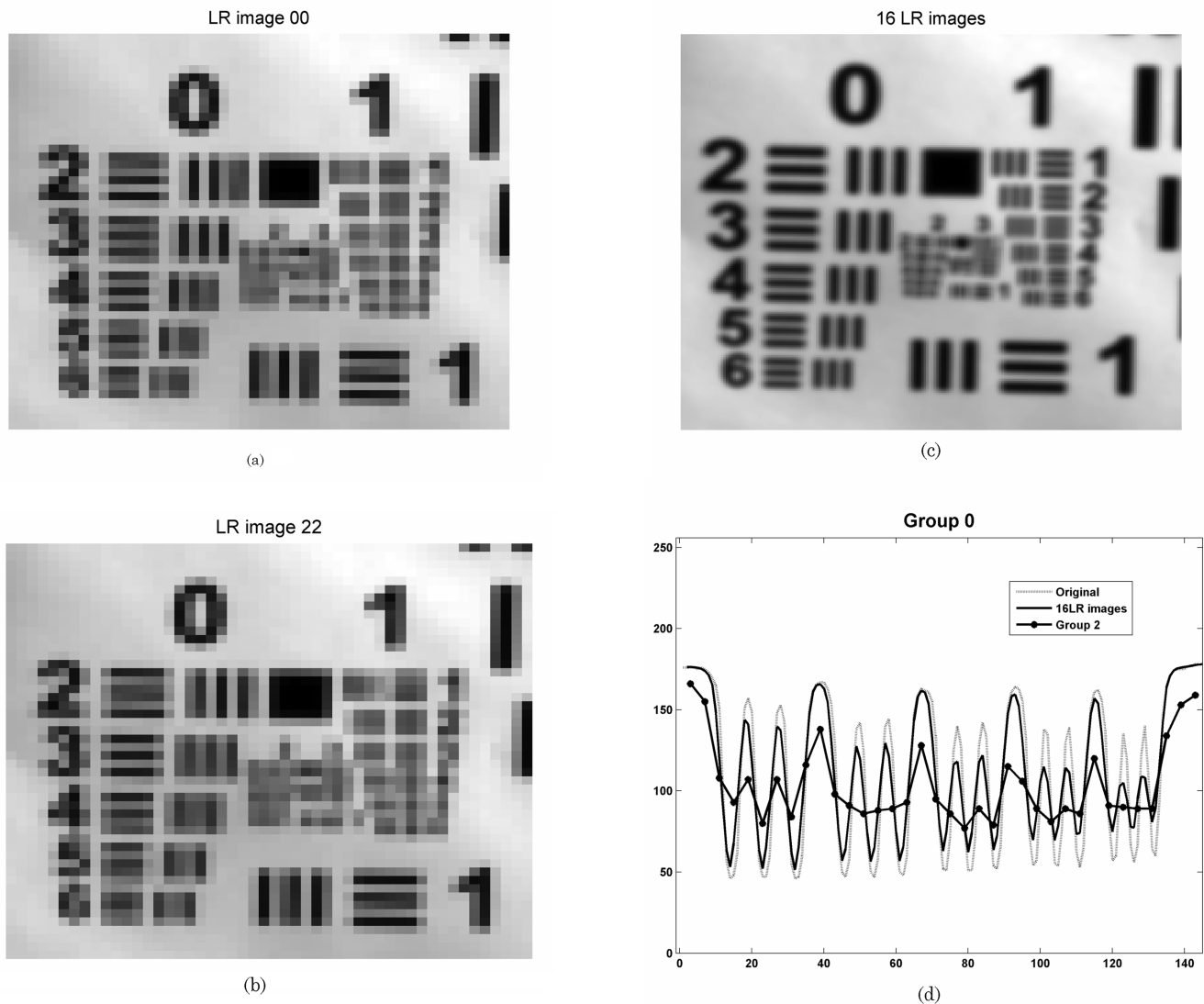


Fig. 3. (a, b) Two  $50 \times 50$  LR images of groups 0 and 1 after resolution is reduced by a factor of 4. (c) Aligned and up-sampled  $200 \times 200$  pixel combination of 16 LR images. (d) Comparison of vertical intensity profiles through group 0 in images in Figs. 2(b) and 3(c) and group 2 in Fig. 2(c).

variety of detector types, the analysis that follows assumes that measurements are normalized so that the maximum measurement value is 1.0, not an integer value determined by the number of bits in the measurement.

The probability distribution for quantization noise is assumed to be uniform over the minimum step size,  $\Delta$ , so the variance is  $\Delta^2/12$ , and it is independent of the measurement value. For normalized pixel values, with  $b$  bits per pixel,  $\Delta = 2^{-b}$ , and the quantization noise variance will be  $(2^{-2b})/12$ . For  $b = 8, 12,$  and  $14$  the quantization variance is  $1.27 \times 10^{-6}, 4.97 \times 10^{-9},$  and  $3.10 \times 10^{-10}$ , respectively.

The variance due to the Poisson arrival process is equal to the mean value of the process, and the number of photoelectrons generated at a detector may be used as an estimate of the mean value for that process. Typically the number of photoelectrons is scaled to provide a specific operating range for measure-

ment values, so the standard deviation associated with the measurement must be scaled by the same factor. Let  $N_i$  be the number of photoelectrons that generates measurement  $g_i$  from a detector with a maximum number of photoelectrons of  $N_{\max}$ . For measurements normalized to provide a maximum value of 1, the scale factor is  $1/N_{\max}$  and  $g_i = N_i/N_{\max}$ . If the mean of the process is  $\bar{N}$ , then the standard deviation of the measurement  $g_i$  will be  $\sqrt{\bar{N}}/N_{\max}$  and the variance will be  $\bar{N}/(N_{\max})^2$ . If it is assumed that  $N_i$  is a good estimate of  $\bar{N}$ , then the variance of a measurement  $g_i$  will be  $g_i/N_{\max}$ . Note that this scaling relationship is consistent with maintaining a typical definition of signal to noise ratio ( $\bar{N}/\sqrt{\bar{N}}$ ). Dividing both the numerator and denominator of the signal to noise ratio by  $N_{\max}$  we have  $(\bar{N}/N_{\max})/(\sqrt{\bar{N}}/N_{\max}) = g_i/(\sqrt{g_i}/N_{\max})$ . Therefore, the variance is  $g_i/N_{\max}$  as derived above.

For example, for  $N_{\max} = 40000$ , the expected variance at the maximum measurement value is  $2.5 \times 10^{-5}$ , and for  $N_{\max} = 100000$  the maximum variance would be reduced to  $10^{-5}$ . For large mean values the Poisson distribution is often approximated as a Gaussian distribution with the same variance. There would be no expected correlation between Poisson distributed noise and the quantization noise.

Additional uncorrelated noise sources can be assumed to have a Gaussian distribution and add additional variance  $\sigma_G^2$  to the measurements. The combined noise for measurement  $g_i$  is  $\eta_i = \eta_Q + \eta_P + \eta_G$  with a total variance of  $\sigma_i^2 = (2^{-2b})/12 + g_i/N_{\max} + \sigma_G^2$ . The variance of the quantization noise is known for a  $b$ -bit measurement and the variance of the Poisson distributed noise can be estimated from the measurement value for known sensor specifications and operational variations. The remaining variance will depend on specific characteristics of the measurement system. Based on this model, a plot of calibration data showing the variance of measurements as a function of their mean values would be expected to be a straight line with a slope of  $1/N_{\max}$  and an intercept of  $\sigma_G^2 + (2^{-2b})/12$ . However, any system variability that causes a scaling difference in the output will increase the slope of the line rather than increase the offset level  $\sigma_G^2$ . For example, variation in illumination level, measurement acquisition time, or other electronics factors could cause additional variance due to scaling changes.

### 3. Image Reconstruction from Multiple Low Resolution Images

Estimating  $f(n_x, n_y)$ , a sampled version of  $f_C(x, y)$  at a desired high resolution sampling rate, requires both an up-sampling operation and a deblurring operation applied to a sequence of LR images as shown in Fig. 1. These two operations may be combined or done separately. Using a measurement model and noise model, an optimal linear estimator performing both operations can be defined. The reconstruction approach described below does not assume regular detector spacing or identical detector geometries, but it does assume that the geometries and field-of-view shifts are known accurately from calibration or active control.

To simplify the mathematical notation for the model of sampled image acquisition and reconstruction, both the observed image pixels,  $g(m_x, m_y)$ , and the desired source pixels,  $f(n_x, n_y)$ , are stored by rows in column vectors  $g(m)$  and  $f(n)$ , where  $0 \leq m \leq M - 1$ ,  $M = M_x M_y$ ,  $0 \leq n \leq N - 1$ , and  $N = N_x N_y$ . Let the  $M \times N$  observation partial matrix,  $H$ , model the linear, but generally space variant, relationship between the desired  $N$  values of  $f$  and the  $M$  observations,  $g$ , from the detector array. The typically used discrete measurement model in Eq. (1) includes an added  $M \times 1$  vector of measure-

ment noise values,  $\eta$ . This model implicitly assumes that the desired sampled image,  $f$ , is an accurate model of the continuous source  $f_C(x, y)$ .

$$g = Hf + \eta. \quad (1)$$

A linear estimate  $\hat{f}$  of  $f$  in Eq. (2) uses an  $N \times M$  reconstruction matrix,  $K$ , where  $f_0$  is the expected value of the vector  $f$  and  $g_0 = Hf_0$  is the expected value of the vector  $g$ . Using a minimum variance of error cost function that minimizes the trace of the expected value of  $(f - \hat{f}) \cdot (f - \hat{f})^T$ , the matrix  $K$  is defined in Eq. (3), where  $R_{fg} = E[(f - f_0) \cdot (g - g_0)^T]$  and  $R_{gg} = E[(g - g_0) \cdot (g - g_0)^T]$ . This optimal minimum variance estimator balances the error introduced by amplifying noise against the error introduced by imperfect inversion of the detector response.

$$\hat{f} = f_0 + K(g - Hf_0), \quad (2)$$

$$K = R_{fg}(R_{gg})^{-1}. \quad (3)$$

If the vector  $f$  were an accurate model of the image source, then, using Eq. (1), Eq. (3) can be written as Eq. (4), where  $\hat{R}_{ff}$  is an estimate of  $E[(f - f_0) \cdot (f - f_0)^T]$ , and  $\hat{R}_{\eta\eta}$  is an estimate of  $E[\eta \cdot \eta^T]$ . The optimal estimator derivation assumes that the noise and source values have Gaussian probability distributions and that there is no correlation between the noise and the source values. For noise values that are independent and identically distributed,  $\hat{R}_{\eta\eta}$  is an identity matrix scaled by the total noise variance  $\sigma^2$ .

$$K = \hat{R}_{ff} H^T (H \hat{R}_{ff} H^T + \hat{R}_{\eta\eta})^{-1}. \quad (4)$$

Let  $f = Az$ , where  $z$  is an  $R \times 1$  vector representing the image source with a higher resolution, so  $R \gg N$ . This is a better approximation of an arbitrary continuous source and is more accurate when partial pixels of  $f$  contribute to measurements. The measurements in Eq. (1) can be written in terms of  $z$  as  $g = H_z z + \eta$ , and the reconstruction matrix can be defined by Eq. (5) where  $\hat{R}_{zz} = A \hat{R}_{zz} A^T$ , but in general  $H_z \neq HA$ . Here  $K_z$  is the same size as  $K$ , but the measurement correlation  $R_{gg}$  is more accurate.

$$K_z = A \hat{R}_{zz} H_z^T (H_z \hat{R}_{zz} H_z^T + \hat{R}_{\eta\eta})^{-1}. \quad (5)$$

The noise model discussed earlier can be used to compute  $\hat{R}_{\eta\eta}$ . In all cases the noise is uncorrelated with the desired image pixel values, so the estimator derivation assumptions are valid if a Gaussian approximation of the distribution can be justified. The variance of the Poisson component for each pixel measurement is proportional to its mean measurement value, but except for small mean values, a Poisson distribution is often well approximated as a

Gaussian distribution with the variance set to the mean value. Thus, when quantization noise variance is substantially lower than the Gaussian and Poisson components, which is the case in the experiments reported here, the total noise can be approximated as a Gaussian distribution. The estimate in Eq. (2) can be used if a reconstruction matrix defined by Eq. (4) or (5) is computed with a new  $\hat{R}_{\eta\eta}$  for each new measurement set. For independent noise components,  $\hat{R}_{\eta\eta}$  is a diagonal matrix with each element equal to the sum of a component proportional to the corresponding measurement value, which estimates the Poisson variance, and a component of constant value, which is a fixed estimate of the Gaussian component and the quantization noise. Since versatile allocation of imaging resources in the PANOPTES architecture [10] requires recomputation of  $K$  for new mirror positions, the new estimate  $\hat{R}_{\eta\eta}$  of can be included in this step.

In simulation, reconstructions from diverse detector array systems with low measurement noise had lower expected errors and demonstrated significantly better definition of low contrast features from an aerial image than systems with a uniform array of the same number of the best detectors [13]. The reconstruction matrices to handle the diverse measurements are a simple extension of the uniform array result, and the reduced null space of the diverse systems allows more local reconstruction with smaller matrix sizes [11–13]. The discrete forms of Eqs. (4) and (5) make no assumptions about uniform detector response, so sets of measurements from detector arrays of different geometry or orientation may be combined to improve the conditioning of the inversion operation. In Eq. (6) the observation vector,  $g$ , is the concatenation of measurements from three different types of subimager arrays, each with its own observation partial matrix and noise covariance. Using the information form of the solution from Eq. (4), the reconstruction matrix  $K$  can be written in terms of the components from each subimager [13] as shown in Eq. (7).

$$g = \begin{bmatrix} g_{\text{I}} \\ g_{\text{II}} \\ g_{\text{III}} \end{bmatrix} = \begin{bmatrix} H_{\text{I}} \\ H_{\text{II}} \\ H_{\text{III}} \end{bmatrix} f + \eta, \quad (6)$$

$$\begin{aligned} K &= (H^T(\hat{R}_{\eta\eta})^{-1}H + (\hat{R}_{ff})^{-1})^{-1}H^T(\hat{R}_{\eta\eta})^{-1} \\ &= (H_{\text{I}}^T(\hat{R}_{\eta\eta\text{I}})^{-1}H_{\text{I}} + H_{\text{II}}^T(\hat{R}_{\eta\eta\text{II}})^{-1}H_{\text{II}} \\ &\quad + H_{\text{III}}^T(\hat{R}_{\eta\eta\text{III}})^{-1}H_{\text{III}} + (\hat{R}_{ff})^{-1})^{-1}H^T(\hat{R}_{\eta\eta})^{-1}. \end{aligned} \quad (7)$$

The expected mean squared error (mse) for any reconstruction matrix  $K$  can be computed as the average of the trace of the expected value of  $\tilde{f} \cdot \tilde{f}^T = (f - \hat{f}) \cdot (f - \hat{f})^T$  as shown in Eq. (8). Since the noise is assumed to be independent of the pixel values, the elements of the matrices  $R_{gf}$  and  $R_{fg}$  are zero, and using Eq. (1), the covariance of the image estimate error can be rewritten in the form of Eq. (9).

$$\begin{aligned} E[\tilde{f} \cdot \tilde{f}^T] &= E[(f - Kg) \cdot (f - Kg)^T] \\ &= R_{ff} - K \cdot R_{gf} - R_{fg} \cdot K^T + K \cdot R_{gg} \cdot K^T, \end{aligned} \quad (8)$$

$$\begin{aligned} E[\tilde{f} \cdot \tilde{f}^T] &= (I - KH) \cdot E[f \cdot f^T] \cdot (I - KH)^T + K \cdot E[\eta \cdot \eta^T] \cdot K^T \\ &= (I - KH) \cdot R_{ff} \cdot (I - KH)^T + K \cdot R_{\eta\eta} \cdot K^T. \end{aligned} \quad (9)$$

In Fig. 4, Eq. (9) is used to compare the expected performance of local image reconstruction of small image sections for four subimager geometries. Reconstruction matrices are computed using Eq. (4) for a specific estimate of noise variance, and the computed mse is plotted against a wide range of actual measurement noise variance values. The values of  $f$  are normalized to have a maximum value of 1. Geometry I uses 16 shifted images from  $9 \times 9$  pixel sensors to compute a  $37 \times 37$  pixel image tile with a linear resolution improvement factor of 4. Two reconstruction matrices for expected noise variances of  $10^{-11}$  and  $10^{-5}$  are tested. These values bracket the quantization noise range for 8-bit and 14-bit data. For actual noise variances below  $10^{-5}$ , the performance is the same for both reconstruction matrices, and reduction of the actual noise variance does not lead to any improvement in the expected reconstruction error standard deviation of 0.111. For higher actual noise variances, the reconstruction matrix that assumed the higher noise level has slightly better performance.

Geometries II and III show the effects of increasing the resolution improvement factor or reducing the size of the local reconstruction. Both have similar performances that are slightly worse than geometry I. Geometry II uses 64 shifted images from  $4 \times 4$  pixel sensors to compute a  $37 \times 37$  pixel image tile with a linear resolution improvement of a factor of 8. Its standard deviation of the reconstruction error in the region of low actual noise variance was 0.165. Geometry III uses 16 shifted images from  $4 \times 4$  pixel sensors to compute a  $17 \times 17$  pixel image tile and had a standard deviation of 0.155 in the region of low actual noise variance.

In contrast, geometry IV uses the same number of observations as geometries I and II to compute a  $37 \times 37$  image tile using  $9 \times 9$  pixel sensors as well as smaller arrays with larger sensors to capture spatial frequencies lost by the smaller sensor. The diversity of this geometry eliminates the null space and allows the reconstruction performance to continually improve by orders of magnitude as the actual measurement noise is reduced until the actual noise variance falls below the value used to create the reconstruction matrix. This behavior allows efficient modular computation by decomposing the large image reconstruction problem into a number of independent small image reconstructions without significant loss of performance. However, as the resolution improvement factor increases, the expected error increases for the same actual noise level [11,13].

Based on the expected performance shown in Fig. 4, if quantization noise were the dominant noise component, then with 14-bit data and a resolution improvement factor of 4, it would be possible to use diversity to advantage and be able to detect very low amplitude image features in a reconstructed image. For a standard deviation of a single quantization level in an 8-bit reconstructed image, the variance would be  $1.5 \times 10^{-5}$ , and the predicted error variance is less than  $10^{-6}$  for 14-bit measurements. This benefit of diversity was demonstrated in simulation for a large aerial image in Ref. [13]. However, with 8-bit measurement quantization, this specific diverse system would only reduce the expected error variance by about a factor of 4 compared to a uniform detector array. When pixel values are scaled to a maximum of 255 for 8-bit data, the standard deviations for the reconstructed images would be approximately 15 and 30, respectively.

#### 4. Analysis of Image Sequences

LR image sequences were collected at VGA resolution with 8 bits and 14 bits per pixel using a Sony XCDV50 black and white camera with a Computar M3Z1228C-MP  $f/2.8$  12–36 mm lens. The detector pixel size was  $7.4 \mu\text{m}$  square. The high contrast 1951 USAF resolution test chart was used as the target in a university laboratory environment. Data from image sequences acquired under both indoor lighting and diffuse external lighting conditions was used to estimate the variance of the three noise components and to explore other sources of variability in the recorded data.

Sequences of images were acquired at 60 frames per second from a tripod mounted camera using a variety of lens settings and camera orientations to estimate the variance of pixel measurements. Figure 2 shows an example of a  $640 \times 480$  pixel image of the computed mean value of a sequence of 300

8-bit images. The variation in light levels in some background areas is due to surface curvature of the chart, which provided a wider range of intensity values. A similar image for 14-bit data acquired under the same conditions is visually indistinguishable, and a scatter plot of the 8-bit mean values versus the 14-bit mean values at corresponding pixel position shows virtually identical results.

A visual presentation of the pixel variance for an image set demonstrates that the variance is proportional to the pixel value. Figure 5(a) displays the variance of the same 300 8-bit frames used in Fig. 2. The white level is set to a variance value  $4 \times 10^{-5}$ . Since the image content is clearly identifiable from the variance image, for most of the image the variance is proportional to the mean value as expected for a significant Poisson distributed noise component. However, the sharp edges of black/white boundaries produce local high variances that appear as bright white edges in the variance image. These high values are attributed to very small movements caused by vibrations in the room. This was tested by analysis of relative shifts within subsets of the data computed using Vanderwalle's method [5]. Most of the images in the sequence were shifted less than  $\pm 0.02$  pixel width of the frame selected as the base image, but this small amount of shift on a sharp edge would increase the variance by an order of magnitude. Sets of 300 frames were divided into smaller sets of 100 frames, and each set was analyzed independently. Results for the smaller sets were similar to each other, so variance was not attributed to any slow drifts in values. The variance image for 14-bit data is also very similar to the 8-bit variance image.

A scatter plot in Fig. 5(b) shows the variance of a set of pixels from areas without pattern edges as a function of their mean values using the same data set used for Figs. 2(a) and 5(a). As predicted by the noise model, the variance values fall close to a straight line showing a significant mean value dependent component of the variance. These image mean values were sorted into 20 equal width bins, and the mean and standard deviation of the variance values for populated bins were computed. The mean values of the variance are shown as light circles, and the standard deviation from the mean is shown with light triangles. The least squares best fit straight line for the mean values has an intercept of  $4.5 \times 10^{-6}$  and a slope of  $4.2 \times 10^{-5}$ , so at the maximum pixel value the variance would be projected to be  $4.7 \times 10^{-5}$  if the measured values did not limit at that level. The 14-bit data had a virtually identical fit with an intercept of  $3.9 \times 10^{-6}$  and a slope of  $4.0 \times 10^{-5}$ .

To further demonstrate the similarity of the 8-bit and 14-bit data, Fig. 5(c) shows histograms for three pixel positions in areas of relatively constant value from 300 8-bit images and from the same pixel positions in 100 14-bit images. For ease of interpretation, both the 8-bit values on the left and the 14-bit values on the right are normalized to a maximum value of 255, and the histogram bin widths are set to 0.25.

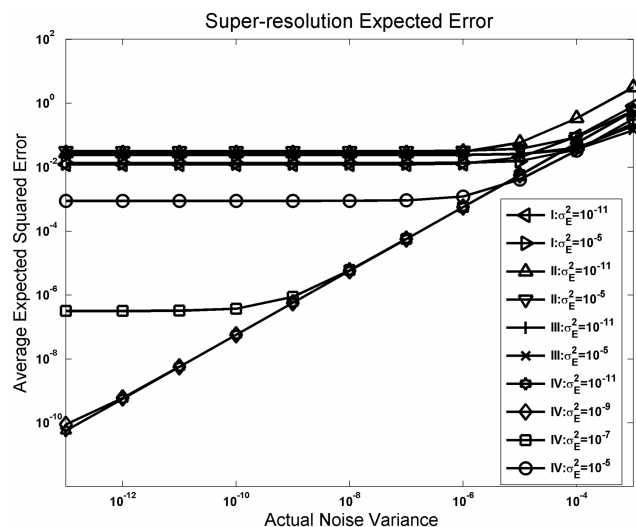
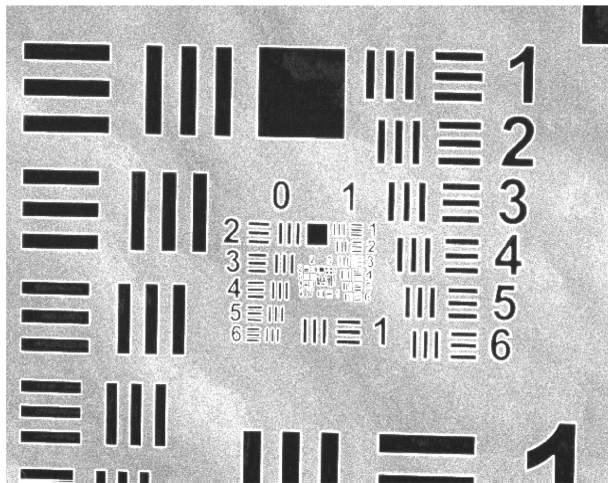
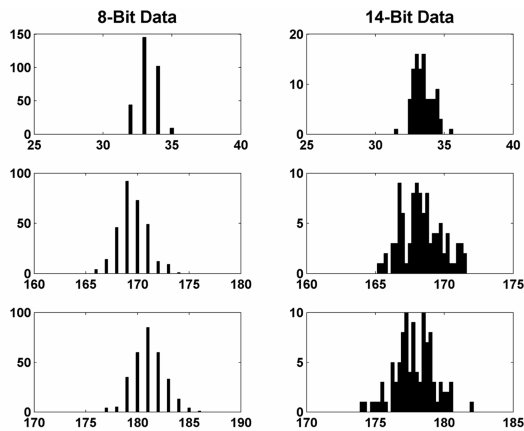


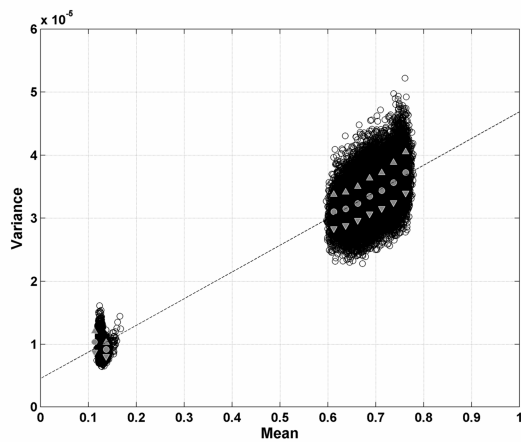
Fig. 4. Expected error as a function of measurement variance for reconstruction matrices for four subimager geometries.



(a)



(b)



(c)

Fig. 5. (a) Variance value of 300  $480 \times 640$  images of 1951 US Air Force resolution test chart; (b) scatter plot of variance versus mean value for a typical set of 300 images from Sony camera; (c) histograms of pixel values at three pixel positions for 8-bit and 14-bit data.

The histograms confirm the dependence of the variance on the mean value and the consistency of the variance for 8-bit and 14-bit data. For the small sample size shown, the histograms are consistent

with a Gaussian approximation for variation about the mean value.

As noted earlier, the maximum expected noise variance due only to a Poisson distributed process with measurements normalized to a maximum value of 1.0 would be  $2.5 \times 10^{-5}$  for  $N_{\max} = 40000$  and  $5.0 \times 10^{-5}$  for  $N_{\max} = 20000$ . The values measured here for mean value dependent variance are within that range, which is reasonable for the type of camera used. Results obtained from numerous experiments using natural lighting on a cloudless day produced similar results. Additional pixel value dependent variance may be caused by small variations in illumination or electronic circuit amplification, which would cause a multiplicative variation in the recorded measurements. For example, an illumination variation with a standard deviation of 1% of a pixel value would add a variance of 0.0001, which is larger than any variances measured. A contribution to variance may also come from the small amount of vibration and the small differences in reflected light levels in areas without pattern edges. In either case, in an operational environment, average illumination level and precise shift offsets could be measured and used to estimate the individual pixel variance values needed to compute the reconstruction matrix.

With maximum noise variance levels around  $5 \times 10^{-5}$ , Fig. 4 predicts an expected error variance of about  $4 \times 10^{-2}$  after restoration, which should allow reconstruction of high contrast edges in an 8-bit result but not low contrast edges. Without the explicit restoration component of the reconstruction, the aligned and interpolated result would show spatial frequency dependent attenuation. However, examination of Eq. (4) for the case of very high measurement noise leads to the approximate expression in Eq. (10), where the reconstruction matrix is approximately proportional to  $H^T$ . This results in a back projected measurement set added to a mean value that can produce a result similar to an up sampled, aligned, and smoothed reconstruction. At this noise level there is no significant improvement expected from using the diverse observations to reduce the null space, and there is very little dependence on the noise level used in the reconstruction matrix. This implies that although each measurement variance depends on the mean signal value for that measurement, the highest of the possible variance values can be used for all measurements without increasing the expected error of the result.

$$K \approx \hat{R}_{ff} H^T (\hat{R}_{\eta\eta})^{-1}. \quad (10)$$

Variable response due to small variations in individual detectors over an array or time varying illumination or circuit behavior will further increase the noise in superresolution applications. The noise variance measured here used a tripod mounted camera, so any differences in individual detector response to the same input were not measured. Since the PANOPTES camera would acquire an image set

simultaneously from multiple arrays, preliminary calibration of detector responses could be used to normalize spatial variability. The time varying illumination problem is solved by simultaneous image acquisition. For sequential image acquisition with shift offsets of several pixels, both temporal and spatial variation must be considered. An additional source of error can come from incorrect shift offset values. In the PANOPTES design, active control of micromirror positions will determine the relative offsets of LR images captured simultaneously, and only fine adjustment of shift position based on image content will be necessary. If shift positions can have large values, the alignment computation may result in larger errors and be more dependent on image content.

To use the single camera to test the benefit of up-sampling and alignment under these noise conditions, sequences of images were captured with small amounts of camera vibration. Algorithms developed by Vandewalle *et al.* [5] were used to estimate the relative shifts for sets of 20 images of the same high

contrast source image. To approximate the expected PANOPTES environment, sets of images with most pixel shifts less than a pixel width were used. Figure 6 shows a representative result. A  $220 \times 220$  pixel portion of a single frame showing groups 2 and 3 and part of group 1 is displayed in Fig. 6(a) and the aligned up-sampled  $880 \times 880$  pixel image is shown in Fig. 6(b). The improvement in all the group 2 elements and the larger group 3 elements is visually obvious, and the background variation is noticeably smoother. The estimated shift offsets are shown in Fig. 6(c), and Fig. 6(d) demonstrates the improvement quantitatively in plots of vertical profiles through group 2 in a manner similar to Fig. 3(d). Two different vertical profiles through a single frame are shown with markers to demonstrate the variability in the undersampled image. The solid curve plot without markers shows the profile for the computed image, and there is almost no variability as the position of this vertical profile is shifted horizontally. Definition of the bars in the smaller elements is not possible from the single frame images, but the

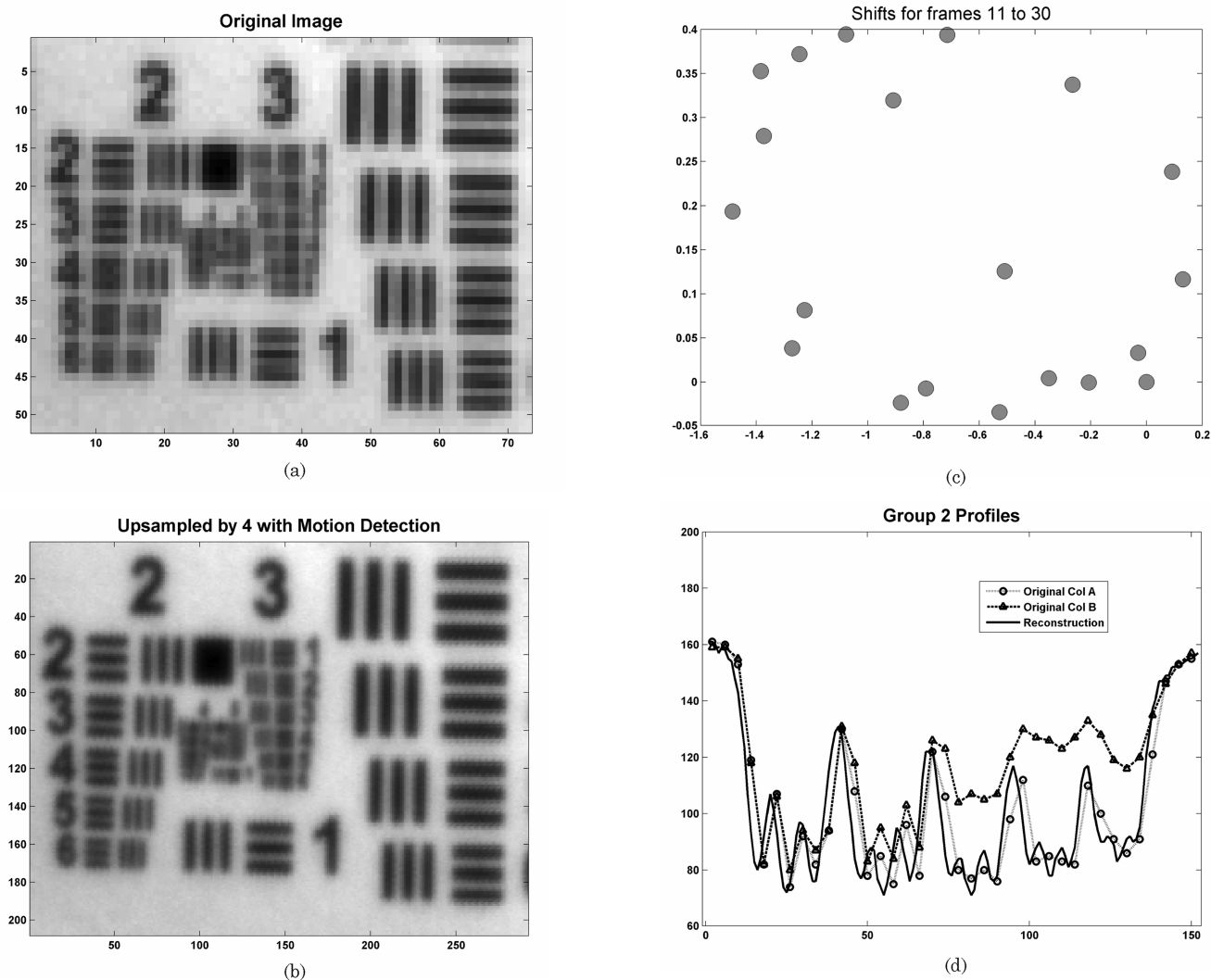


Fig. 6. (a) Single image (b) computed high resolution image from set of 20 image frames; (c) detected relative shift in pixels for 20 frames; (d) plot of vertical intensity profile through group 2 of computed image compared to two columns from a single frame.

bars are defined by pixel value differences of 6% to 12% of the dynamic range for the computed image. Although this difference is reliably detectable, a lower contrast boundary in a source image would be lost. This is consistent with the results shown in Fig. 4.

## 5. Conclusions

This paper has explored the effect of measurement noise due to quantization and Poisson and Gaussian processes on previously reported theoretical results for superresolution image reconstruction using uniform and nonuniform detector array geometries. This is compared to measurements taken from a commercial camera that provides 8-bit and 14-bit data. With nonuniform detector arrays structured to reduce or eliminate the null space of uniform detector arrays, the expected error variance of the reconstruction is reduced as the number of bits of information in the measurements is increased. In contrast, uniform arrays have an observational null space, and at some level further reductions in measurement noise will not result in reduced expected reconstruction error.

The reconstruction matrix that minimizes the expected error of the HR image computed from multiple LR images depends on accurate models of the detector response and orientation as well as estimates of the noise variance and variance of the image class. These distributions are assumed to be Gaussian. The measurement noise is shown to be reasonably approximated by a Gaussian distribution if the quantization noise, which is uniformly distributed, has a variance significantly lower than other noise components, and if the mean measurement values are large enough for the Poisson noise component to be approximated by a Gaussian distribution with the same variance. Under these conditions, a reconstruction matrix can be computed for each data set with the variance for each measurement determined by the measurement value. For the PANOPTES architecture with agile allocation of subimager resources, frequent recomputation of the reconstruction matrix would be required as viewing directions change, so adjusting the noise variance estimate could be included in this computation.

Simulations of optimal linear reconstruction matrices for several examples of uniform and nonuniform arrays predict that reducing the measurement noise variance below  $10^{-5}$  for the uniform array structures would not reduce the expected error of the result and also that the expected error below this level is insensitive to the noise variance estimate. However, because of the null space associated with uniform arrays, the actual reconstructed error can be strongly dependent on image content. Analysis shows that the variance for 8-bit and 14-bit measurements from the camera tested is almost exactly the same, with the measurement variance increasing linearly with the mean value of the measurement as expected for a significant Poisson contribution. The highest variance value, which approaches  $5 \times 10^{-5}$ ,

is approximately equal to the expected quantization noise for 6-bit data.

A number of conclusions can be drawn from these results. For a camera with noise characteristics similar to those observed here, the largest component of the measurement noise is proportional to the mean value of the measurement and is determined by the number of photoelectrons generated at the detectors and any other multiplicative factors. In comparison, quantization noise due to 8-bit measurements is not significant. This is not surprising for cameras designed to produce images primarily for human viewing since the human visual system can discriminate somewhere between 100 and 200 distinct gray levels in an image. At these noise levels the improvement expected from nonuniform detector arrays is small, but the sensitivity of the expected error to the noise variance estimate is also small, so the largest variance value could be used for all measurements. For random processes, variance can be reduced by averaging independent observations, and in this application additional images could be acquired for that purpose. If nothing else changes, this is equivalent to increasing the number of photoelectrons generated by a smaller number of measurements. However, simultaneous acquisition of LR images is advantageous because any uncalibrated time variation in illumination levels will increase the measurement noise level.

The expected error level of computed HR images determines how much contrast is needed in the image source for accurate detection of reconstructed image features. Continued improvement in the reduction in the expected error requires detectors with lower measurement variance and detector arrays designed to minimize the null space of the measurements. As the noise is reduced, the dependence of the reconstruction matrix on correctly estimated noise variances will increase. Each measurement value can be used to predict the Poisson component of its measurement variance, which is approximated as a Gaussian distribution with the same variance, and the reconstruction matrices can be computed from those estimates.

The authors gratefully acknowledge the support of the U.S. Army Research Laboratory for this effort through collaborative technology agreement award W911NF-06-2-0035.

## References

1. S. Chaudhuri, ed. *Super-Resolution Imaging* (Kluwer Academic, 2001).
2. M. Elad and A. Feuer, "Restoration of a single superresolution image from several blurred, noisy, and undersampled measured images," *IEEE Trans. Image Process.* **6**, 1646–1658 (1997).
3. M. Elad and Y. Hel-Or, "A fast super-resolution reconstruction algorithm for pure translational motion and common space invariant blur," *IEEE Trans. Image Process.* **10**, 1187–1193 (2001).

4. S. Farsiu, D. Robinson, M. Elad, and P. Milanfar, "Fast and robust multiframe super-resolution," *IEEE Trans. Image Process.* **13**, 1327–1344 (2004).
5. P. Vandewalle, S. Süsstrunk, and M. Vetterli, "A frequency domain approach to registration of aliased images with application to super-resolution," *EURASIP J. Appl. Signal Process.* **2006**, 71459 (2006).
6. D. Robinson, S. Farsiu, and P. Milanfar, "Optimal registration of aliased images using variable projection with applications to superresolution," *Comput. J.* (April/May 2007).
7. J. Tanida, T. Kumagai, K. Yamada, S. Miyatake, K. Ishida, T. Morimoto, N. Kondou, D. Miyazaki, and Y. Ichioka, "Thin observation module by bound optics (TOMBO): concept and experimental verification," *Appl. Opt.* **40**, 1806–1813 (2001).
8. Y. Kitamura, R. Shogenji, K. Yamada, S. Miyatake, M. Miyamoto, T. Morimoto, Y. Masaki, N. Kondou, D. Miyazaki, J. Tanida, and Y. Ichioka, "Reconstruction of a high-resolution image on a compound-eye image-capturing system," *Appl. Opt.* **43**, 1719–1727 (2004).
9. K. Nitta, R. Shogenji, S. Miyatake, and J. Tanida, "Image reconstruction for thin observation module by bound optics by using the iterative backprojection method," *Appl. Opt.* **45**, 2893–2900 (2006).
10. M. P. Christensen, V. Bhakta, D. Rajan, S. C. Douglas, S. L. Wood, and M. W. Haney, "Adaptive flat multiresolution multiplexed computational imaging architecture utilizing micro-mirror arrays to steer subimager field of views," *Appl. Opt.* **45**, 2884–2892 (2006).
11. S. L. Wood, B. J. Smithson, D. Rajan, and M. P. Christensen, "Performance of a MVE algorithm for compound eye image reconstruction using lens diversity," *IEEE International Conference on Acoustics, Speech and Signal Processing* (IEEE, 2005), Vol. **II**, pp. 593–596.
12. S. L. Wood, Hsueh-Ban Lan, D. Rajan, and M. Christensen, "Improved multiplexed image reconstruction performance through optical system diversity design," *IEEE International Conference on Image Processing* (IEEE, 2006), p. 2717.
13. H.-B. Lan, S. L. Wood, M. P. Christensen, and D. Rajan, "Benefits of optical system diversity for multiplexed image reconstruction," *Appl. Opt.* **45**, 2859–2870 (2006).
14. R. N. Bracewell, *Two-Dimensional Imaging* (Prentice-Hall, 1995).
15. A. Macovski, *Medical Imaging Systems* (Prentice-Hall, 1983).
16. Z.-H. Cho, J. P. Jones, and M. Singh, *Foundations of Medical Imaging* (Wiley, 1993).
17. S. L. Wood, G. Yang, M. P. Christensen, and D. Rajan, "Effect of measurement precision on super-resolution image reconstruction", presented at the OSA Topical Meeting on Computational Optical Sensing and Imaging (COSI), Vancouver, British Columbia, 18–20 June 2007..
18. S. Mitra, *Digital Signal Processing*, 3rd ed. (Prentice-Hall, 2006).
19. A. Jain, *Fundamentals of Digital Image Processing* (Prentice-Hall, 1989).